

An Acoustic Remote Sensing and Submersible Study of an Arctic Submarine Spring Plume

EUGENE B. COLBOURNE¹ AND ALEX E. HAY

Department of Physics, Memorial University of Newfoundland, St. John's, Newfoundland, Canada

Results from a field study of a submarine spring and its associated brackish water plume at the head of Cambridge Fiord, Baffin Island, are presented. Computer-enhanced 1920-kHz acoustic backscatter images yield measures of maximum height of rise, plume geometry, and vertical velocities in the rising plume. Submersible observations indicate that the freshwater discharge is localized, being about 5 m in horizontal extent. A thriving benthic community was found within this area. The initial geometry and water properties of the flow at the vent, together with the ambient stratification and a numerical buoyant plume model, are used to show that the probable freshwater discharge rate lies in the range 0.10 to 0.20 m³/s. Computed vertical velocities on the plume axis are significantly greater than the vertical velocities inferred from scattering structure trajectories in the acoustic images. The decay of acoustic backscatter amplitude as a function of radial distance in the neutrally buoyant spreading plume is comparable to the radial decay of temperature fine structure, and the radial decay scales are consistent with those expected from molecular dissipation of turbulent microstructure.

1. INTRODUCTION

Submarine springs and their associated plumes have not been studied extensively. An informative review of early work has been written by Kohout [1966]. Most known springs have been discovered either because of some surface signature [e.g., Blume *et al.*, 1981] or by scuba divers. These observations are usually possible only in shallow water. There is evidence, however, to suggest that freshwater discharge can occur at depths as great as 500 m [Manheim, 1967], and it might be expected that more evidence for deepwater springs will accumulate as the use of submersibles, remote operated vehicles, and modern underway survey techniques becomes more extensive.

The submarine spring at the head of Cambridge Fiord, Baffin Island, was discovered because aerial reconnaissance photographs revealed the annual formation, in late winter, of a polynya approximately 50 m in diameter [Dunbar, 1958]. Sadler and Serson [1980] reported the first direct observations of the polynya and were the first to suggest that it was caused by a submarine freshwater spring. The source of groundwater feeding the spring was believed to be the lake shown in Figure 1, because the water level of this lake decreases by approximately 1.0 to 2.0 m during the winter, when there is no surface runoff at these latitudes. Furthermore, Sadler and Serson found that the discharge rate equivalent to this drop in lake level was comparable to the submarine spring discharge rate needed to form and maintain the polynya. Subsequently, Hay [1984] reported the results of a preliminary study of the discharge plume, in which acoustic sounding techniques were used to locate and monitor the plume during the ice-free season in autumn, when the plume did not reach the surface.

In this paper, results from a third investigation of the submarine spring and buoyant plume in Cambridge Fiord are

reported, including the first direct observations of the vent itself. The purpose of the study was to determine the physical nature of the vent, to quantify the freshwater discharge rate, and to further investigate the relationships between acoustic backscatter and turbulent fine structure in the plume. Our interest in the latter problem stems from the fact that acoustic remote sensing techniques are being used increasingly in connection with a variety of small-scale physical processes in the ocean, and in many instances it has been suggested that turbulent microstructure may contribute to the observed backscatter. Examples include large-amplitude interfacial waves [Prøni and Apel, 1975; Haury *et al.*, 1979; Farmer and Smith, 1980], and high-temperature hydrothermal plumes [Palmer and Rona, 1986]. However, the relative contribution to these acoustic images of scattering from turbulence, and from biological or other scatterers often found in association with thermocline or pycnocline zones [e.g., Kaye, 1979], has proved difficult to resolve in most instances. Nevertheless, several studies have shown theoretically that the scattering cross sections for turbulence quantities in the ocean can in some circumstances be comparable to typical cross sections for biological organisms [Munk and Garrett, 1973; Prøni and Apel, 1975; Goodman and Kemp, 1981]. Finally, clear evidence for the detection of turbulent microstructure by acoustic backscatter has been obtained in the field in studies of turbulent wakes generated by towed or self-propelled objects in the presence of stratification, with the observed cross sections exhibiting good agreement with theoretical calculations [Pelech *et al.*, 1983; Thorpe and Brubaker, 1983].

This paper begins with a presentation of the data from a 3-day experiment in 1985, including the acoustic imagery and submersible observations, which are both used to characterize the discharge and the geometry of the plume. The submersible observations are also of interest biologically, since they revealed the presence of a productive community of benthic organisms localized to the discharge area. The discharge and plume observations are then compared to results from a numerical plume model in order to determine the probable rate of freshwater discharge. This is followed by a comparison between measured backscatter amplitudes

¹Now at Department of Fisheries and Oceans, St. John's, Newfoundland, Canada.

Copyright 1990 by the American Geophysical Union.

Paper number 90JC00208.
0148-0227/90/90JC-00208\$05.00

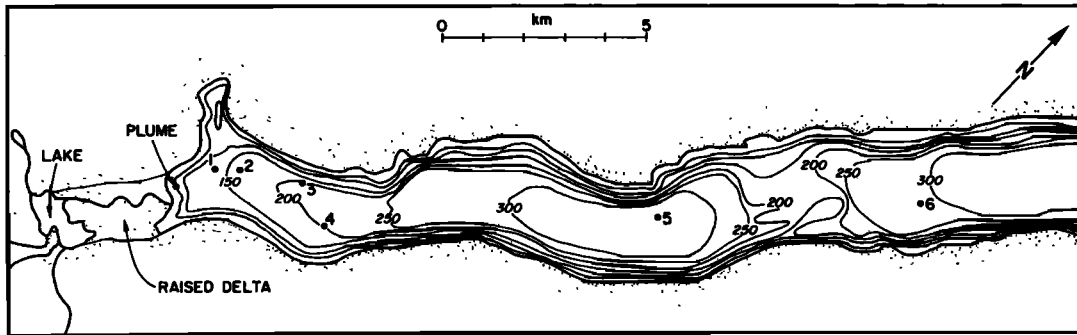


Fig. 1. Bathymetric chart of the head of Cambridge Fiord, showing the location of the submarine spring. The position of the lake thought to be the source of the spring is also shown. Depths are in meters.

and temperature and salinity fine structure and by a discussion of the implications of this comparison for sound scattering by turbulence in the plume. Finally, a brief discussion of the effects of the submarine spring on the local biological community is presented.

2. THE STUDY AREA AND METHODS

Cambridge Fiord is situated on the east coast of Baffin Island, at approximately 71°N, in the Canadian Arctic archipelago. The fjord reaches inland for about 100 km and has a low tidal range, typically less than 1 m. The bathymetry in the area near the head of Cambridge Fiord is shown in Figure 1. The previously mentioned freshwater lake is located approximately 3 km from the head on the delta, which has risen through time, as a consequence of isostatic rebound, to its present height of about 30 m above sea level. The lake is drained by a seasonal stream, which has cut a channel through the raised delta. Results from a study of the plume in September 1985 from the *Pandora II* and the submersible *Pisces IV* are reported here, together with some results from an earlier study in September 1983 aboard the C.S.S. *Hudson* [Petrie and Trites, 1984].

The 1985 field program was restricted to observations of the plume and the ambient environment at the head of the fjord. Four dives on the site were made with *Pisces*. The plume was located with the ship's launch using the 192-kHz acoustic sounder described below. Navigation on board *Pisces* was based on acoustic direction finding to a pinger at the freshwater vent, which had been deployed from the launch. Measurements made with *Pisces* included velocity, with a Neil Brown Instruments Systems DRCM-2 acoustic current meter; conductivity and temperature, using a Guildline model 8770 portable conductivity-temperature-depth profiler (CTD); and visual and photographic observations, using a Photosea 2000 camera and an Osprey video camera system. Water samples for laboratory analysis were taken using the submersible's suction water sampler.

The plume was mapped from the launch by running acoustic sounding lines in circular arcs spaced at approximately 10-m intervals in the general area of the vent. The arcs were centered on microwave shore transponders, which were part of a Motorola Miniranger microwave positioning system, having a rated accuracy of 1 to 2 m. Two transponders were deployed on the beach, separated by 229 m.

The acoustic sounder was built by Ross Laboratories, Inc. The transmitted output power is 800 W rms, the receiver

sensitivity is 0.65×10^{-6} V over a bandwidth of 5 kHz, and the transducer beamwidth is 2.3°. The sounder was operated with a pulse length of 0.5 ms, giving a range resolution of approximately 40 cm, and with a pulse repetition interval of 270 ms. The full-wave rectified, low-pass-filtered acoustic backscatter signals were FM recorded on a Racal Store 4DS instrumentation tape recorder. The recordings were made at a tape speed of 38.1 cm/s, for which the recorder's frequency response was flat from 0 to 5 kHz, -3 dB at 6.2 kHz, and -20 dB at 10 kHz. The rms tape noise level was approximately -43 dB at 3 kHz. Each analog tape was calibrated by recording the 3 DC levels from the recorder's calibrator output. The analog signal was digitized on a HP model 5451B Fourier analyzer at an effective rate of 40 kHz by using a playback tape speed at 19.1 cm/s and a sampling rate of 20 kHz. The recorded trigger pulse was used to activate a 4096-point digitizing window. Acoustic images of the plume were constructed from the acoustic data using a Norpak VDP-11 image-processing system.

The plume was also mapped with a closely spaced grid of CTD stations, by hand-hauling the launch from station to station while it was tied to a four-point mooring. The Guildline CTD system (sampling interval of 190 ms) was also mounted in a fixed position on *Pisces* during the submersible dives. For the current measurements from *Pisces*, the DRCM-2 acoustic current meter (0.5-s sampling interval) was mounted on the submersible's remote manipulator arm. Measurements were made while the submersible was resting on the seabed. The current meter was maintained in a roughly horizontal orientation by the pilot, using spirit levels mounted to the current meter pressure case. This was not always a straightforward operation, however, as the submersible had a tendency to sway as the manipulator arm moved, because of the uneven seabed. The deck unit for the DRCM was modified so that the orthogonal velocity components could be obtained instead of the usual components referenced to magnetic north, which were of no value in this application.

3. OBSERVATIONS

Figure 2 shows temperature, salinity, and σ_θ along an axial section at the head of the fjord in September 1983. Although these data were not collected during the main experiment in 1985, they provide a general picture of the ambient stratification in the fjord in the autumn. A low salinity, roughly 2°C upper layer of the order of 10 m thick, is separated from cold

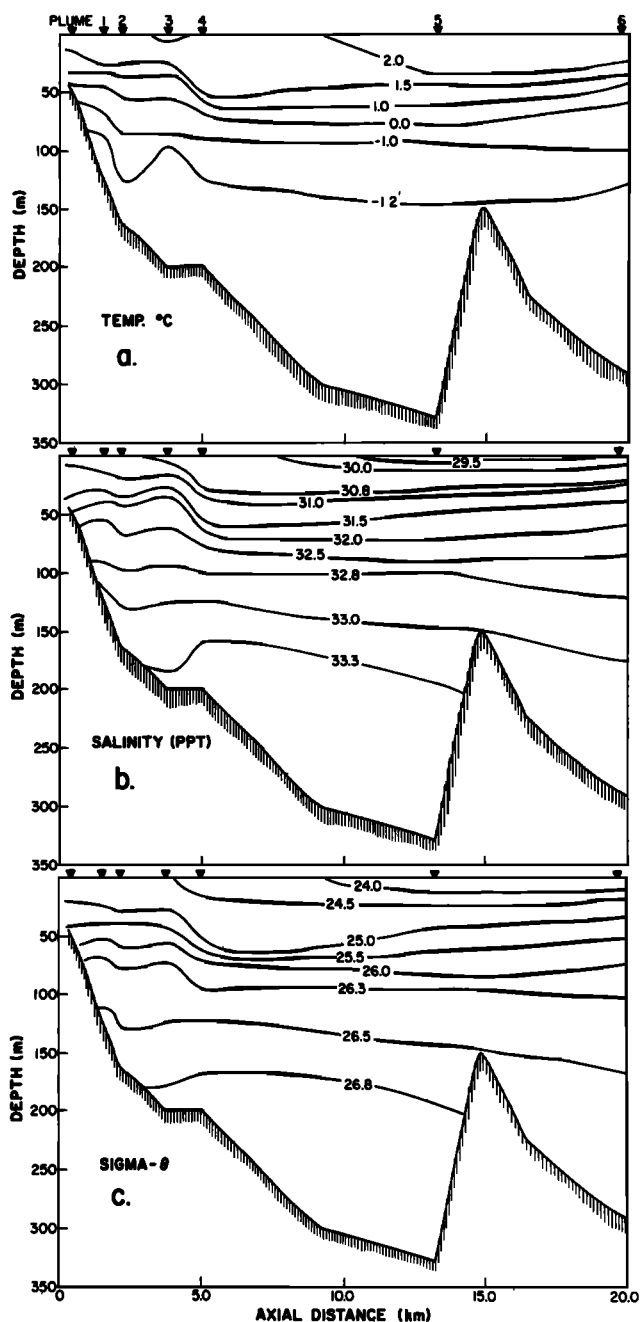


Fig. 2. Vertical sections of temperature, salinity and σ_t at the head of the fjord, from 1983.

(subzero) temperatures at depths below 75 m, by a pycnocline 50 to 70 m thick. The ambient temperature and salinity around the vent area in 1983 were approximately 0.0°C and 31.5 at 50 m depth.

Figure 3 shows the detailed bathymetry in the vent area and was constructed from the soundings at all position fixes obtained during the acoustic sounding survey of the plume. The offshore coordinate is the perpendicular distance from the beach, and the alongshore coordinate is the distance along the beach in a northwestward direction. The position of the vent is indicated by the X on the 47-m isobath. The bottom slope is about 10° in the general area of the vent. The dashed lines represent acoustic sounding transects to be discussed later. The solid squares and triangles indicate

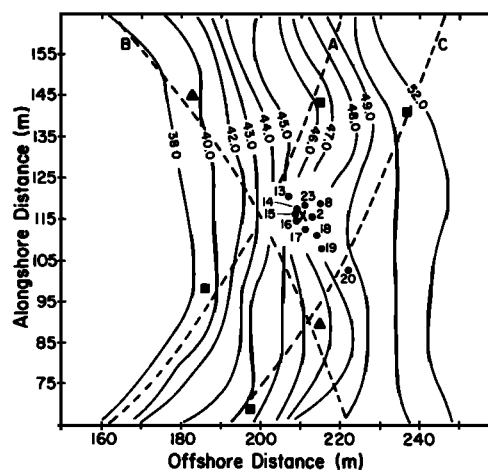


Fig. 3. Bathymetric chart of the vent area. Position fixes are marked by the solid squares and triangles. The CTD stations are indicated by solid circles. The dashed lines represent acoustic sounding transects. The X marks the position of the vent.

position fixes along each of the three transects shown. The squares correspond to fixes along transects centered on the northern transponder, the triangles to a transect about the southern transponder. The dashed lines shown are circular arcs centered on the appropriate transponder, with radii corresponding to the average radius computed from all fixes (typically 4 or 5) along each transect. Positions of CTD stations discussed below are also indicated.

Temperature, salinity, and σ_t sections through the plume, constructed from stations 13 to 20 (Figure 3), are presented in Figure 4. The CTD data were first averaged over 1.0 m in the vertical before these sections were constructed. This eliminates fine-scale variations and makes the spreading plume difficult to distinguish. The rising plume is clearly visible, however: the salinity at 40 m depth near the plume axis is less than 30.0, as compared to values greater than 30.7 just outside the plume area; and a tongue of lower-salinity water (less than 30.0) is seen to extend upward from the bottom. The top of the plume coincides with the base of the pycnocline at about 10 to 12 m depth. These sections indicate that the plume is about 6 m wide at 30 to 40 m depth. This is consistent with the horizontal profile of temperature and vertical velocity through the plume obtained in 1983 [Hay, 1984], which indicated a width of about 8 m at a depth of 33 m.

3.1. Acoustic Imagery

Plate 1 shows color-coded acoustic images constructed from the digitized acoustic backscatter signals acquired along transects A, B, and C in Figure 3. (Plate 1 is shown here in black and white. The color version can be found in the separate color section in this issue.) These images have been enhanced by thresholding to remove the background noise level and by contrast stretching (by which the maximum signal amplitude assigned a color is reduced to increase the resolution of the color representation). In these images, red represents high signal level, detector saturation is black, and the background level is white. The horizontal scale, determined from the average speed of the launch along each transect (about 1.3 m/s), is 70 to 80 m/min.

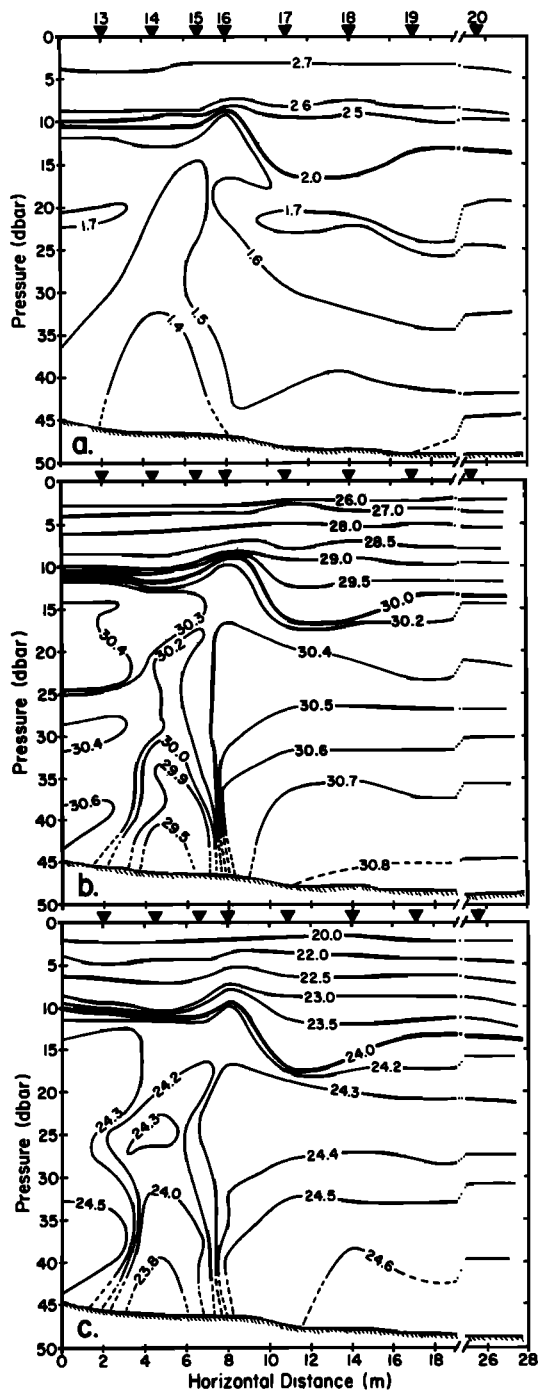


Fig. 4. Vertical sections of (a) temperature, (b) salinity, and (c) σ_t through the plume. The total elapsed time between the beginning of the first CTD cast and the end of the last on the transect shown was 1 hour 10 min.

The narrow, approximately vertical, rising plume can be seen in Plates 1a and 1b, which correspond to transects A and B in Figure 3. The plume reaches its maximum height of rise at 15 to 17 m depth and then falls back to spread radially outward along approximately horizontal surfaces at depths of 20 to 30 m. In this horizontally spreading part of the plume, the backscatter amplitude decreases with radial distance from the rising plume axis. The image shown in Plate 1c was acquired along transect C (Figure 3), which is

farther to one side of the vent. The rising plume is not present, and the spreading plume is between 20 and 27 m depth. Tongues of plume water are again seen to be spreading out along vertically separated, approximately horizontal surfaces. Similar images obtained in 1983 [Hay, 1984] show the plume extending from the bottom up to a minimum depth of 9 m and spreading out horizontally between 12 and 20 m depth. These differences in the maximum height of rise, and in the depth of the spreading plume, are due to different ambient stratification during the 2 years. The greatest difference in this respect is that the brackish upper layer was both thicker and less saline in 1985 (compare Figures 2 and 4). Differences in height of rise are also observed from day to day: for example, the rising plume in Plate 1 reaches a depth of 15 m, while the CTD data in Figure 4, which were collected the following day, show the plume reaching 10 m depth. This is due to a change in the ambient stratification in response to a reduction in the speed of up-inlet winds [Colbourne, 1987].

There is a near-bottom zone of high amplitude backscatter in the acoustic images in Plate 1. Large numbers of euphausiids were observed from the submersible near the bottom and are thought to be responsible for this feature. The undulations in this zone, particularly evident in Plate 1a, are due to the launch rolling in 1 to 2 m seas. Similar undulations can be seen at the top of the rising plume in Plate 1a. The appearance given by Plates 1a and 1b of more than one closely spaced rising plume is also due to this wave-induced launch motion, which would have caused the sounder's beam to swing in and out of the rising plume.

Plate 2 shows depth versus time color-coded images of the plume, obtained while the launch was four-point moored over the vent. (Plate 2 is shown here in black and white. The color version can be found in the separate color section in this issue.) The echo from the CTD instrument package can be seen in these images as an oblique trace during ascent and descent and as a horizontal trace at depth. Image E corresponds to station 2P in Figure 3, and shows discrete scattering structures rising from the near-bottom zone at approximately constant speed, and then decelerating above 20 m depth. Maximum ascent rates calculated from the slopes of these trajectories in the 20- to 37-m depth range are about 32 cm/s. These results are similar to those reported by Hay [1984]. Image F shows a similar image, recorded at a lower receiver gain than image E, corresponding to station 23 in Figure 3. These images were obtained the day after those in Plate 1, and it can be seen that the maximum height of rise increased by 5 m as was discussed previously.

The ascending scattering structures are intermittent, with an average recurrence interval of about 0.5 min. The nature of the scattering structures is still not fully understood and is discussed later. The oscillations in plume height, particularly in image F, have periods of about 3 min. These periods are typical of internal waves. This suggests that the oscillations arise because of coupling between the ambient stratification and the rising plume through the internal wave field.

The acoustic image G was obtained with the launch four-point moored over the spreading plume. The descending CTD probe entered the top of the plume at about 12 m depth and emerged at about 20 m depth. The horizontally coherent structures seen below 25 m in the first 1.5 min of the image disappear as the CTD descends, producing the relatively scatter-free region after the CTD has passed. This

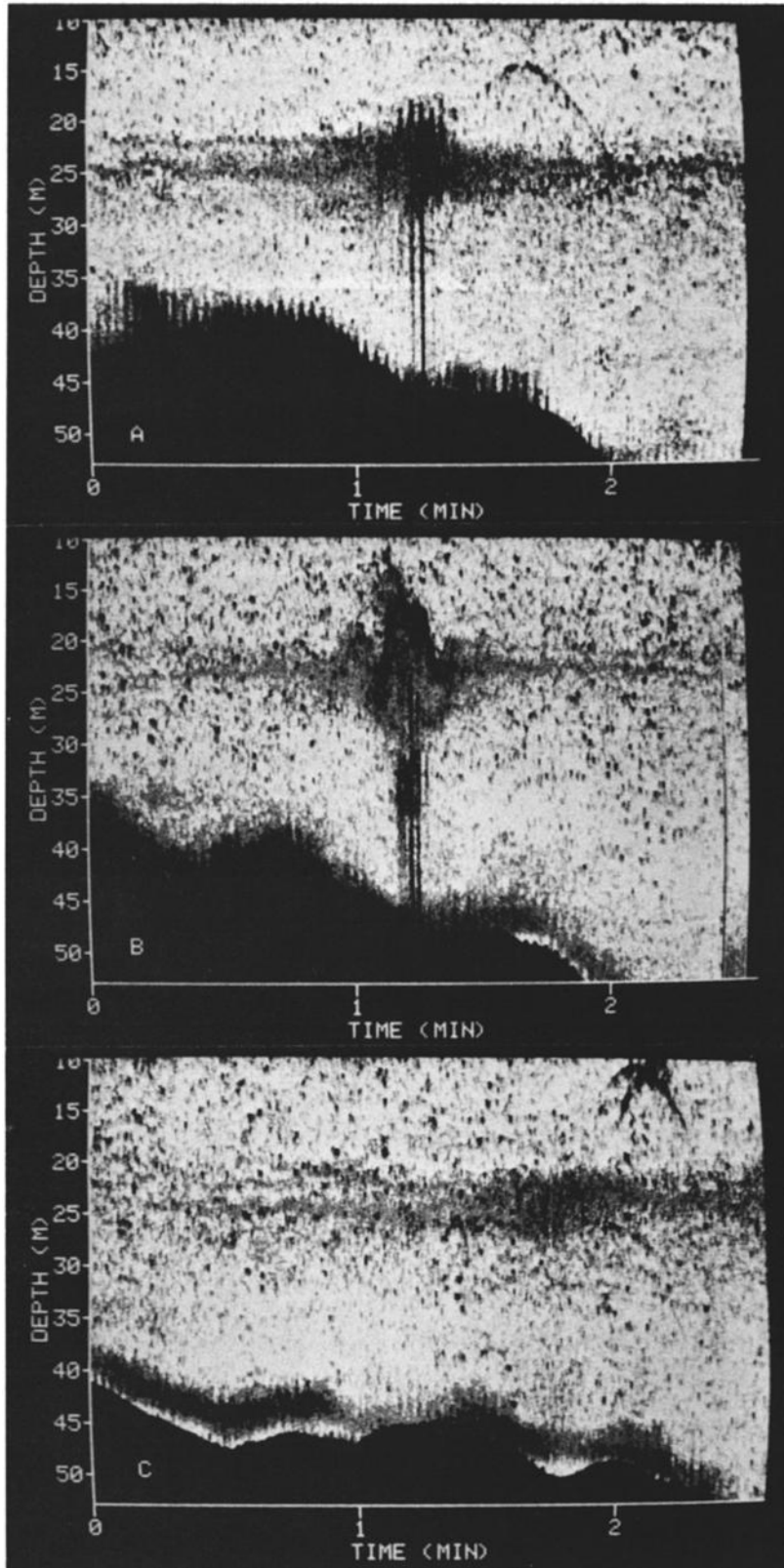


Plate 1. Color-coded images of the plume corresponding to acoustic transects A, B and C in Figure 3. (The color version and a complete description of this figure can be found in the separate color section in this issue.)

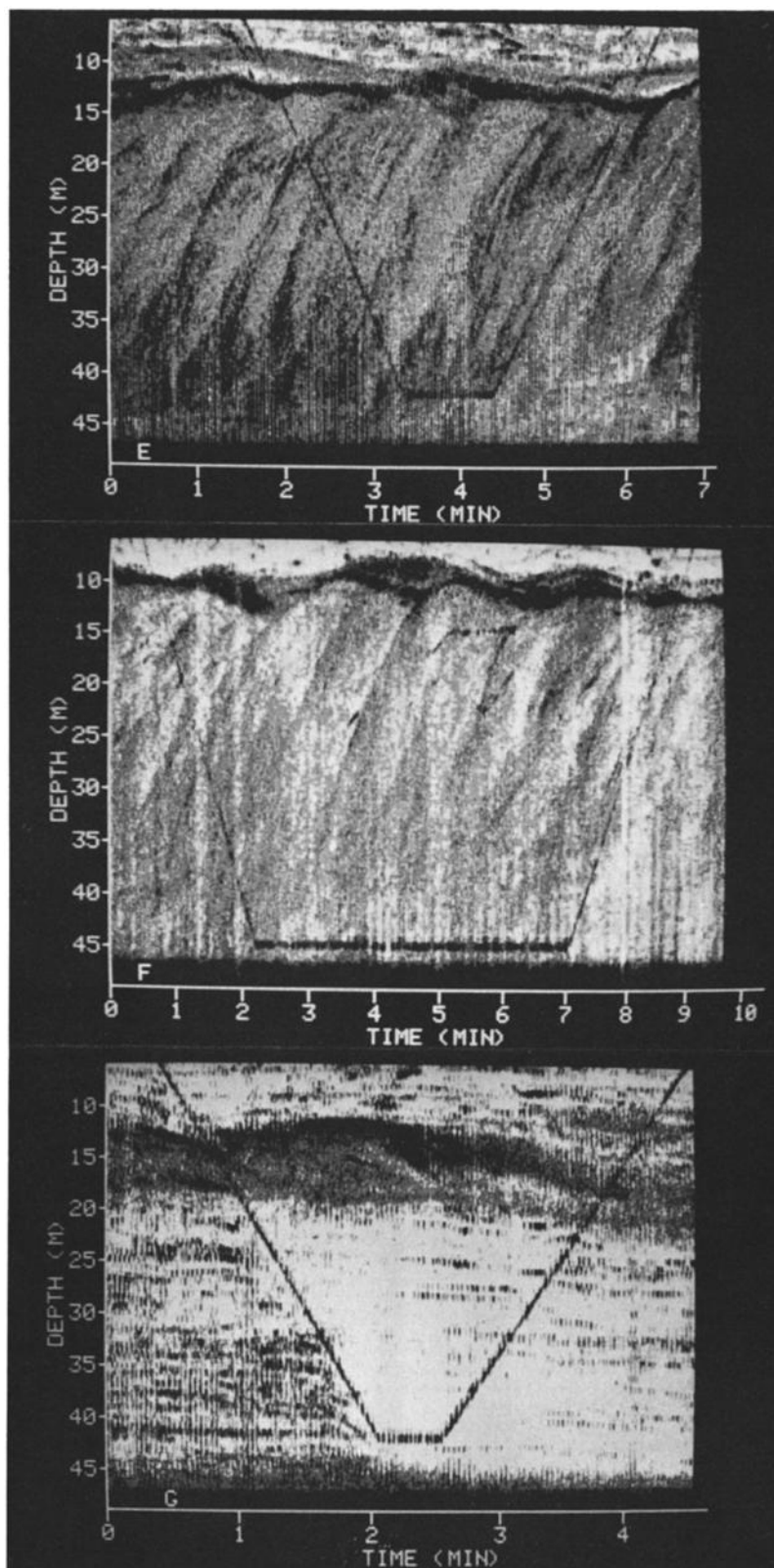


Plate 2. Depth versus time color-coded images of the plume obtained while the launch was four-point moored over, and to one side of, the vent. Images E and F show acoustic images within the rising plume (CTD stations 2P and 23). Image G is an image of the spreading plume (CTD station 8). (The color version of this figure can be found in the separate color section in this issue.)

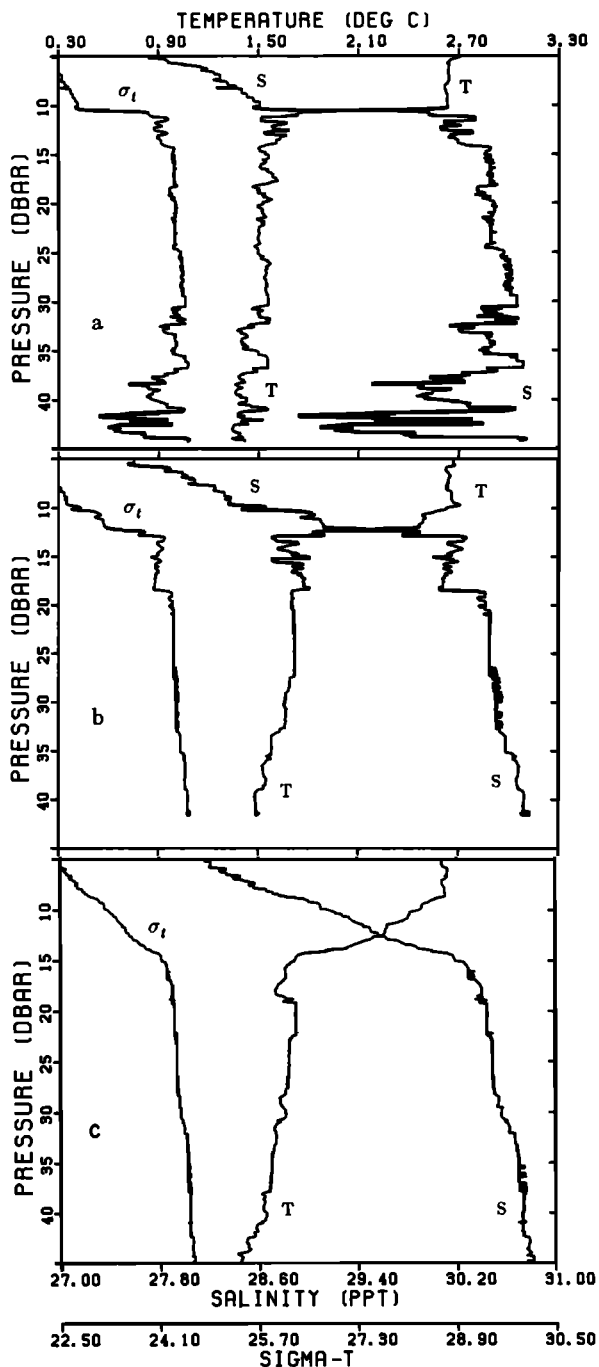


Fig. 5. (a) CTD profile through the rising plume corresponding to station 23 and acoustic image F in Plate 2. (b) CTD profile through the spreading plume corresponding to station 8 and acoustic image G in Plate 2. (c) Ambient CTD profile obtained outside the plume at station 20.

indicates to us that the disappearing scatterers are biological organisms, which move to avoid the descending CTD package.

3.2. CTD Profiles

Figures 5a and 5b show temperature, salinity, and σ_t profiles obtained at station 23 over the vent and at station 8 over the spreading plume (see Figure 3 for station locations). These profiles correspond to acoustic images F and G in

Plate 2. Figure 5c shows the ambient vertical structure at station 20, which is well away from the rising plume (Figure 3).

Figure 5a is typical of the CTD profiles through the rising plume. As was discussed previously with respect to Figure 4, the base of the pycnocline is at about 10 m depth. Above this depth, there is a brackish isothermal layer extending to the surface, with high salinity and density gradients. Spikes in the salinity and density profiles are seen at about 7.5 m depth. These spikes are artificial and are due to the time-constant mismatch between the temperature and conductivity sensors and their physical separation on the CTD probe. The top of the rising plume occurs at about 11 m depth (Plate 2, image F) and is marked by abrupt changes in all three profiles. The amplitude of fine structure variations, many of which are statically unstable, increases with depth below this point. Minimum salinities of about 29 are present near the bottom of the profile. This fine structure is not artificial: it is due to the fresh water being discharged from the submarine spring.

The profiles in Figure 5b correspond to the CTD cast through the spreading plume in acoustic image G in Plate 2. Again we have a brackish, nearly isothermal, upper layer about 10 m thick with high salinity and density gradients. Artificial spiking is again evident in this region. Large amplitude variations in temperature and salinity occur where the CTD enters the spreading plume at 12 m depth (Plate 2, image G). Below the 12- to 20-m depth range the profiles are relatively smooth. The thickness of the spreading plume, as indicated by the sharp interface at 12 and 18 m depth in this profile, compares well with the thickness observed in acoustic image G, about 8.0 m.

The density profile in Figure 5c does not show the large amplitude statically unstable features that are evident within the rising plume. There is an indication of the spreading plume in the temperature profile at depths of 15 to 20 m. The σ_t profile in Figure 5c is used to represent the ambient stratification in the numerical plume model discussed later.

3.3. Submersible Observations

The submersible dives show that the discharge, rather than being a point source, is in fact distributed over an area roughly 5 m in diameter. Within this area, the fresh water was observed to be seeping slowly from the bottom, with virtually no initial momentum. This suggests that the groundwater feeding the discharge is percolating through the delta. However, a large rock about 2 m long by 0.7 m wide by 0.5 m high was sitting in the middle of the discharge area (see the sketch in Figure 6), and the nature of the freshwater discharge underneath the rock is not known. The discharge mixture converges toward the rock in the centre of the vent area, and combines with several other smaller discharge plumes to form a single plume of brackish water approximately 1.0 m above the bottom.

Figure 7 is a photograph of part of the discharge area. The right-hand side of the photograph is blurred by variations in optical refractive index caused by the mixing of fresh water with the ambient seawater. The photograph also shows anemones on the rocks bathed in the discharge plume water. Kelp, scallops, and other organisms were also found. Elsewhere, away from the vent, the benthic fauna are comparatively very sparse, indicating that the submarine spring

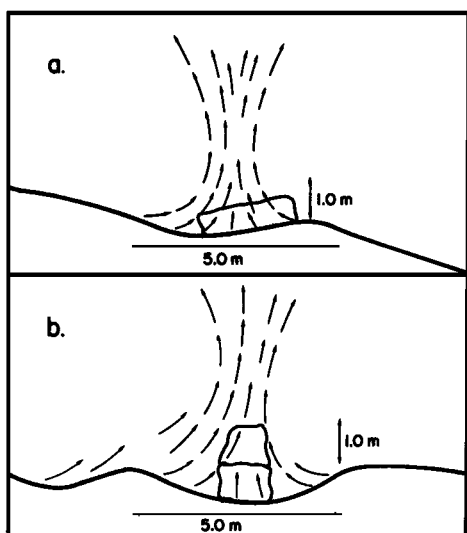


Fig. 6. Sketch of the vent area. (a) Onshore-offshore view. (b) Alongshore view.

system supports a benthic community which is highly productive relative to the immediate vicinity.

Samples of the discharge water, obtained a few centimeters above the bottom using the suction sampler mounted on the submersible's manipulator arm, yielded salinities of 17 to 29. A short distance from the actual discharge, values of 30.9 to 31.6 were obtained, consistent with the CTD measurements made from the launch.

Figure 8a shows a typical time series of temperature, salinity and σ_t obtained from *Pisces* with the CTD probe over the rock at about 1.5 m above bottom. The mean temperature and salinity from this time series are 0.8°C and 27.7 respectively. Note the large fluctuations, particularly in salinity. Minimum salinities of less than 23 are present. These minimum salinities are comparable to the minimum value of 17 determined from the water samples. The mean time interval between large amplitude fluctuations is of the order of 0.5 min in this record, which is comparable to the

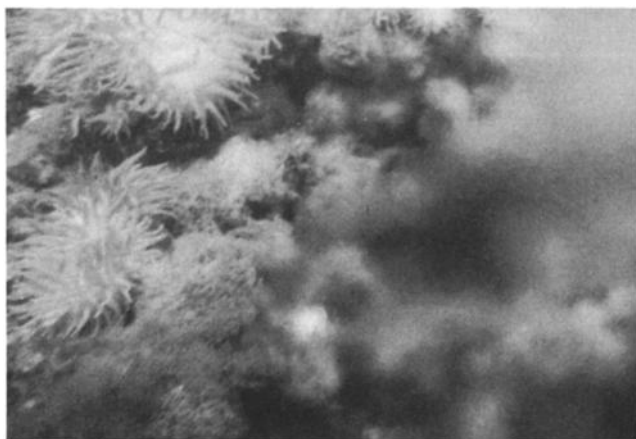


Fig. 7. Photograph of the vent area taken from within the submersible *Pisces IV*. This photograph shows the anemones found around the vent area. The blurring effect caused by the freshwater discharge can be seen on the right. The anemones (10 to 20 cm across) provide a rough scale.

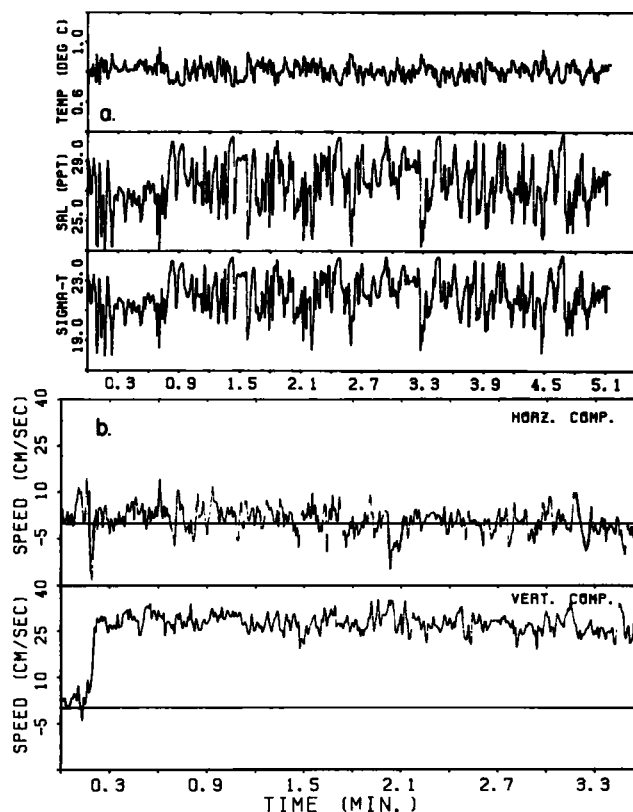


Fig. 8. (a) Time series of temperature, salinity and σ_t ; and (b) horizontal and vertical velocities obtained at the vent from the submersible about 1 m from the bottom.

mean interval between the rising scattering structures seen in the acoustic images in Plate 2.

Time series of horizontal and vertical velocity components, from approximately the same location as the CTD time series in Figure 8a, are shown in Figure 8b. The horizontal velocity component fluctuates around zero. Fluctuations of the order of 10 cm/s are observed, with an average amplitude of about 4.0 cm/s. Any movement of the submersible during the measurements would have contributed to this variability. However, a review of the section of videotape corresponding to this particular time series indicated no obvious submersible motion relative to the bottom. The vertical component fluctuates around a mean of 30 cm/s after the current meter probe was inserted into the rising plume at 0.2 min. relative time. These measured speeds compare well to the near-bottom value of 32 cm/s estimated from the acoustic images.

4. DISCUSSION

4.1. Comparison With Plume Models

To simulate the rising plume, we used the numerical model developed by *Ditmars* [1969] using the integral technique of *Morton et al.* [1956] for an axisymmetric buoyant plume in a stagnant stratified fluid. This problem has been reviewed by *Turner* [1973, 1986], *Fischer et al.* [1979], and *List* [1982].

The terminal height of rise of a buoyant plume depends on the ambient stratification, the buoyancy flux B , and momentum flux M at the source. Considering the special case where the initial momentum flux is very small compared with the buoyancy flux, the terminal height of rise depends only on

the ambient stratification and B and is given by [Fischer *et al.*, 1979, p. 342]

$$h_B = C_1 \frac{B^{1/4}}{(N^2)^{3/8}} \quad (1)$$

where N is the buoyancy frequency in the ambient fluid. The coefficient of proportionality, C_1 , was determined from experimental data by Morton *et al.* [1956] to be about 3.8. Similarly if we consider the other limit as $B \rightarrow 0$, the flow will approximate a simple momentum jet, and the terminal height of rise in this case is given by

$$h_M = C_1 \left[\frac{M}{N^2} \right]^{1/4} \quad (2)$$

The ratio of these two length scales h_M/h_B raised to the eighth power can be considered to be the defining parameter for buoyant plumes in a stratified fluid [Fischer *et al.*, 1979, p. 343]. After substituting for the momentum and buoyancy fluxes, this ratio becomes

$$\hat{S} = \frac{\rho_0^2 U_0^2 N^2}{(g\Delta\rho)^2} \quad (3)$$

where $\Delta\rho$ is the initial density difference between the ambient fluid and the plume, and U_0 is the discharge velocity.

We take the starting point for the plume to be at 1 m above bottom: that is, above the rock and the near-bottom convergent flow. We wish to estimate the value of \hat{S} at this point. A linear fit to the ambient density profile below the pycnocline (Figure 5c) gives a buoyancy frequency of $9.8 \times 10^{-3} \text{ s}^{-1}$ and an ambient density at 46 m of 1025 kg/m^3 . Taking a discharge salinity of 28, which is typical of the CTD measurements from the submersible in the vicinity of the rock (Figure 8a), gives $\Delta\rho \approx 2.8 \text{ kg/m}^3$, and with an initial discharge velocity U_0 of 30 cm/s, $\hat{S} = 0.012$. We therefore conclude that the plume is dominated by buoyancy at our chosen starting point.

The governing equations in the numerical model are the conservation equations for volume, momentum, and buoyancy, integrated across the width of the plume, assuming Gaussian velocity and density defect profiles, and can be written as

$$\frac{d}{dz} (Ub^2) = 2\alpha_0 Ub \quad (4)$$

$$\frac{d}{dz} \left(\frac{U^2 b^2}{2} \right) = g\lambda_s^2 b^2 \frac{(\rho_a - \rho)}{\rho_0} \quad (5)$$

$$\frac{d}{dz} (Ub^2(\rho_a - \rho)) = \frac{1 + \lambda_s^2}{\lambda_s^2} b^2 U \frac{d\rho_a}{dz} \quad (6)$$

where z is the vertical coordinate, α_0 is an entrainment coefficient, ρ_a is the ambient density, b is the jet width defined below, and U and ρ are the centerline velocity and density respectively. These equations have been discussed in detail by Turner [1973] and Fischer *et al.* [1979]. The reference density ρ_0 is taken as the value of the ambient density at $z = 1.0 \text{ m}$; that is, 1025 kg/m^3 . The turbulent Schmidt number λ_s^2 is defined as the ratio of the width of the density defect profile to the width of the velocity profile. It is

a measure of the plume's ability to disperse density relative to momentum. As was suggested by Morton [1959], λ_s is set equal to 1.16. The entrainment coefficient α_0 is set equal to 0.082 [Fan and Brooks, 1969; Turner, 1986]. The three unknowns U , b , and ρ , are functions of the vertical centerline coordinate only. In the Ditmars model, these equations are integrated numerically by Runge-Kutta-Gill methods until the vertical velocity vanishes or becomes very small.

The required inputs for the model are the initial diameter, the initial velocity, the ambient stratification, and the initial density difference. However, we can specify only the initial velocity, ambient stratification, and the initial density difference. We do not have a measure of the initial diameter, and furthermore, the rate of freshwater discharge is unknown. These two quantities are related, through the total discharge rate, as follows. The initial salinity and the volume rate of discharge can be found by considering the sum of the freshwater discharge and the seawater entrained into the discharge. This entrainment certainly occurs in the convergence zone near the bottom, and may also include entrainment of saline porewater within the prodelta itself. We assume here that the salinity of both types of entrained water is the same. The initial salinity of the discharge mixture can then be written as

$$S_0 = \frac{S_e Q_e}{Q_f + Q_e} \quad (7)$$

where S_e and Q_e are the salinity and volume transport of entrained water, and Q_f is the rate of freshwater discharge. The total initial discharge rate $Q_0 = Q_f + Q_e$ can now be written as

$$Q_0 = \frac{S_e Q_f}{S_e - S_0} \quad (8)$$

The effective initial diameter D_0 of the discharge region is then related to the total discharge rate and the initial velocity by $Q_0 = \pi U_0 D_0^2/4$, and is thus given by

$$D_0 = \left(\frac{4Q_f S_e}{\pi U_0 [S_e - S_0]} \right)^{1/2} \quad (9)$$

The initial diameter D_0 is therefore the so-called top-hat value, determined from volume flux considerations. The numerical model assumes fully developed flow at the source, and therefore Gaussian profiles of mean velocity and density defect, and the nominal plume width is defined as 4 standard deviations (4σ) of the velocity profile [Ditmars, 1969]. Equating the top-hat volume flux (Q_0 above) to that given by a Gaussian velocity profile, we obtain $4\sigma = \sqrt{2}D_0$ for the initial width. S_e and U_0 were set equal to 31.6 and 30 cm/s, respectively.

The model was run for a range of initial discharge salinities (S_0) and freshwater discharge rates (Q_f), using (9) to compute the initial diameter. Figure 9a shows computed plume widths as a function of height, for a range of initial salinities, and a fixed freshwater discharge rate of $0.15 \text{ m}^3/\text{s}$. The average maximum height of rise as determined from the Ross sounder records, 35 m, is also shown. It can be seen that an initial salinity of 29 is too high for this value of Q_f because the plume does not reach the observed height. It can also be seen that as the initial salinity decreases, the maximum

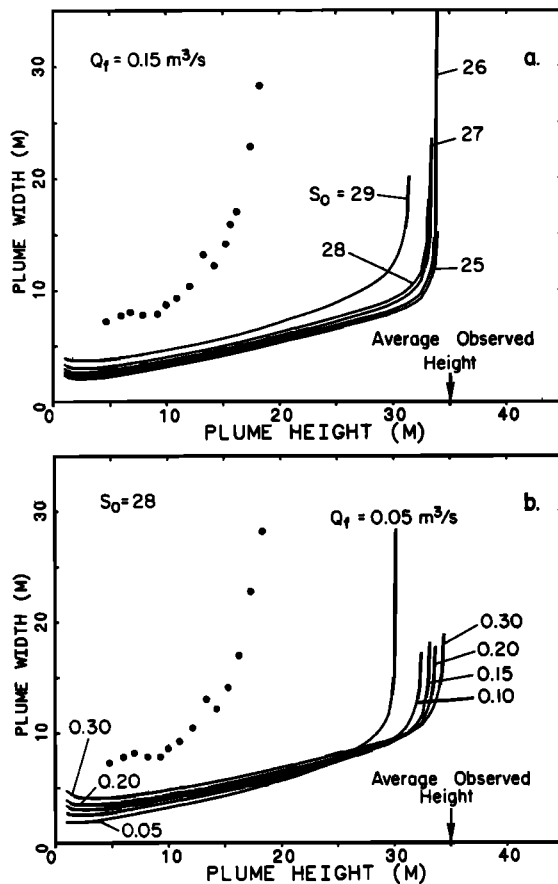


Fig. 9. (a) Model plume widths versus height for different S_0 and fixed $Q_f = 0.15 \text{ m}^3/\text{s}$, and (b) for different Q_f and fixed $S_0 = 28$. The average observed maximum height of rise is indicated by the arrows, and the measured plume widths are shown by the solid circles.

height of rise becomes insensitive to initial salinity, which is expected because of the capping effect of the near-surface, low-salinity layer (Figures 4 and 5). This happens for initial salinities less than or approximately equal to 28.

Figure 9b shows computed plume widths for an initial discharge salinity of 28 and for a range of freshwater discharge rates. This initial salinity is close to the mean salinity of 27.7 in the CTD time series in Figure 8a, which was obtained at the vent with the submersible. It is clear that values of Q_f below about $0.10 \text{ m}^3/\text{s}$ are too small for this initial salinity, since the plume does not reach the observed height. The maximum height of rise is not very sensitive, however, to values of Q_f above $0.10 \text{ m}^3/\text{s}$. The initial width, however, does impose an upper limit on the freshwater discharge. Although it was not possible to obtain an accurate measure of the initial width from the submersible, our visual observations certainly showed that the initial width was less than 5 m. Consequently, the results in Figure 9b indicate that values of Q_f of $0.3 \text{ m}^3/\text{s}$ and greater are too large. (For completeness we ran the model to determine the freshwater discharge required to pierce the thermocline and reach the surface. For $S_0 = 28$ and $U_0 = 30 \text{ cm/s}$, this value turned out to be about $20 \text{ m}^3/\text{s}$, 2 orders of magnitude larger than the maximum possible freshwater discharge rate estimated above.)

Plume widths estimated from the acoustic sounding sur-

vey are also shown in Figure 9. These were determined from a total of nine acoustic transects, which were used to construct horizontal cross sections of the rising plume as a function of depth. These cross sections were not circular: for example, that at 23 m depth was approximately 80 m wide in the alongshore direction and about 45 m wide in the offshore direction [Colbourne, 1987; Colbourne and Hay, 1987]. Nevertheless, we define a characteristic plume width as the square root of the cross-sectional area. Plume widths were determined from the horizontal maps in this way at 1-m depth intervals from 18 to 42 m depth, which corresponds to heights above bottom between 5 and 29 m. For heights below 10 to 12 m, the measured widths show roughly the same increase with height as the computed widths for freshwater discharge rates between 0.10 and $0.20 \text{ m}^3/\text{s}$. However the observed widths within this height range are almost twice as large as the computed values. We believe that this is mainly due to an increase in the apparent width caused by the rolling of the launch. A roll angle of $\pm 3^\circ$ about the vertical would produce a doubling of the apparent width from 4 m to 8 m at 40 m depth, and certainly the 3- to 5-m undulations in the apparent range of the near-bottom scattering layer in Plate 1a imply at least this much roll (± 4 to 7° , in fact). At heights greater than 12 m the observed widths become very large compared with those given by the model. This is due to the finite thickness of the spreading plume, which affects the observations but is not included in the numerical results, and due to the previously mentioned 5 m lower plume height during the acoustic sounding survey.

It would appear that for an initial salinity of 28 which, to reiterate, was close to the value of 27.7 measured from the submersible, the freshwater discharge must fall in the range 0.10 to $0.20 \text{ m}^3/\text{s}$ to be consistent with our observations. This range is surprisingly close to the value of $0.14 \text{ m}^3/\text{s}$ obtained by Sadler and Serson [1980]. They obtained their estimate from heat budget considerations associated with maintenance and growth of the polynya. While their heat budget argument was made assuming that there was no entrainment of seawater into the rising plume, which the present study shows is clearly incorrect, the discharge rate of $0.14 \text{ m}^3/\text{s}$ is consistent with the observed drop of 1 to 2 m in the water level of a lake situated 3 km from the head of the fjord (Figure 1). Because this decrease in lake level occurs during winter when there is no surface runoff, they attributed the decrease to discharge via the submarine spring.

Figure 10 shows vertical profiles of centerline velocity predicted by the model, for the same range of initial salinities and freshwater discharge rates as Figure 9. These profiles do not exhibit the constant vertical velocity in the 5- to 25-m height range that might have been expected on the basis of the rising scattering structures in Plate 2 (image E), and which have also been reported elsewhere [Hay, 1984]. Furthermore, the velocities computed for the most probable values of initial salinity (28 or less) and freshwater discharge (0.10 to $0.20 \text{ m}^3/\text{s}$) are much higher in this height range than the 32 cm/s determined from the scatterer trajectory slopes. This perhaps implies that the scattering structures are located not on the centerline of the rising plume, but instead toward its edge where the mean velocity is lower, and consequently that the scattering structures may be associated with eddies formed at the edge of the plume.

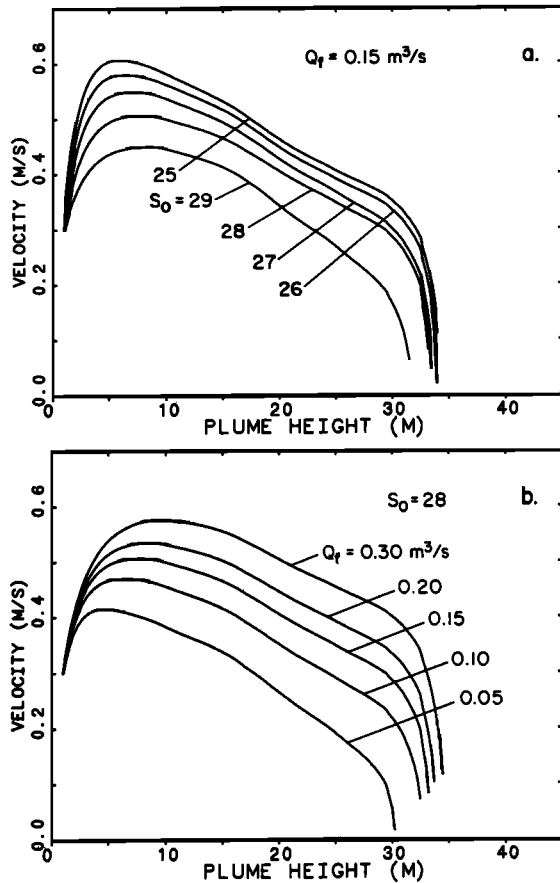


Fig. 10. (a) Model centerline velocity profiles for the rising plume with Q_f fixed at $0.15 \text{ m}^3/\text{s}$ for a range of initial salinities, and (b) with S_0 fixed at 28 for a range of freshwater discharge rates.

4.2. Radial Decay of Fine Structure and Backscatter in the Spreading Plume

We now investigate the possibility that turbulent fluctuations may be at least partially responsible for the observed backscatter from the plume. There are a number of reasons for supposing that this could be true. The submersible observations at the vent showed that the water escaping from the bottom is clear and free of gas bubbles and suspended sediments. In 1983, when the plume reached the surface (after an overnight period of surface cooling), no suspended sediments or bubbles were observed.

In order to investigate this problem further, we consider the decay of backscatter amplitude within the spreading plume, as a function of radial distance from the plume axis, as seen, for example, in the acoustic images in Plate 1. The question we wish to consider is whether or not the observed rate of radial decay is consistent with turbulent microstructure being the dominant backscatter mechanism. The coarse resolution of the CTD probe does not allow this question to be answered directly, and we are therefore forced to make indirect arguments. These are presented below.

Acoustic backscatter due to turbulence arises from acoustic refractive index fluctuations with spatial scales of half the acoustic wavelength λ [Tatarski, 1961]. Turbulent velocity fluctuations cannot by themselves contribute to backscatter. The refractive index fluctuations are proportional to the ratio

of the sound speed fluctuation c' to the mean speed c_0 , which at 0°C and a salinity of 30 is

$$\frac{c'}{c_0} \approx 3.2 \times 10^{-3} T' + 9.2 \times 10^{-4} S' - 3.7 \times 10^{-5} T'^2 \quad (10)$$

using the sound speed relation given by Mackenzie [1981], where T' and S' are the temperature and salinity fluctuations. We see that the salinity contribution is somewhat smaller than that of temperature and that the T'^2 terms are negligibly small for temperature fluctuations of the order of 1°C or less.

It is of interest to determine the minimum turbulence microscale, which can be related to the dissipation rate ϵ [Tennekes and Lumley, 1972, pp. 20 and 240]. In the steady state the supply rate of energy from large- to small-scale eddies is equal to ϵ , which can be estimated from the mean flow to be $\rho\epsilon = \rho(U^3/2L)$, where U is the mean flow speed and L is the spatial scale of the largest eddies. If we take L in the rising plume to be of the order of half the plume width, or about 5 m, and use a measured velocity of 30 cm/s, we find that $\rho\epsilon$ is approximately 3 W/m^3 . For seawater the diffusivities of heat and salt are respectively $\gamma_T \approx 10^{-7} \text{ m}^2/\text{s}$ and $\gamma_S \approx 10^{-9} \text{ m}^2/\text{s}$ [Gill, 1982, pp. 68 and 71]. Using these values, the temperature and salinity microscales are 0.04 and 0.004 mm, respectively, which are much smaller than $\lambda/2$ (3.9 mm at 192 kHz). We therefore conclude that temperature and salinity microstructure should be present at scales corresponding to $\lambda/2$ and thus could contribute to the observed acoustic backscatter.

4.3. Observations of Radial Decay

Root-mean-square fine structure variations in temperature and salinity were obtained by high-pass filtering the CTD data. The filter used to generate fine structure profiles had a cutoff frequency of 0.3 Hz, which, with the 0.35 m/s descent rate of the CTD (determined from the slope of the probe echo in the acoustic images) corresponds to a (upper) cutoff vertical scale of about 1 m. The minimum vertical scale resolvable by the CTD depends on the sensor size and time constant. For temperature, for which the time constant of the sensor is rated by the manufacturer at 60 ms, the minimum scale at the above descent rate is about 2 cm, which is of the same order as the physical size of the sensor. Since the sampling rate was 190 ms, fluctuations with spatial scales between 13 and 2 cm are aliased in the temperature profiles. The rms temperature and salinity fluctuation amplitudes were computed over a time interval corresponding to the range resolution of the sounder, about 40 cm. This interval was chosen in order to compare the rms fluctuations in temperature and salinity with rms acoustic backscatter amplitude at the same depth.

The acoustic backscatter profiles were averaged over five consecutive pings, providing an effective time average over about 1.35 s at a given depth, and vertically averaged over the pulse length (about 40 cm). The acoustic backscatter signals were corrected for spreading and attenuation by applying a correction factor

$$F = \frac{r}{r'} \exp [2\alpha(r - r')] \quad (11)$$

such that $v' = v_{\text{rms}} F$, where v_{rms} is the measured rms backscatter amplitude. The r terms in (11) correct for spread-

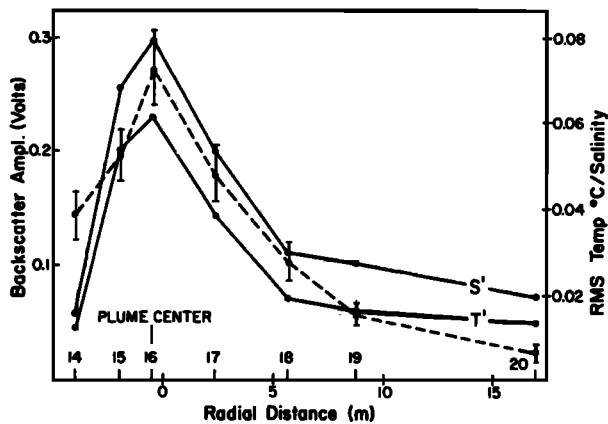


Fig. 11. Root-mean-square acoustic backscatter amplitude (dashed line) and temperature and salinity rms fine structure versus radial distance from the plume axis, from stations 14 to 20. Station 16 is nearest the center of the plume. The error bars represent 1 standard deviation from the means.

ing of the transmitted pulse and attenuation of the transmitted and backscattered signal. No spreading correction is applied to the scattered return because the scatterers are assumed to be uniformly distributed throughout the beam at a given range. The r' terms represent a renormalization factor used to retain the unit volts for the corrected signal: r' was set equal to one-half the total water depth. The attenuation coefficient α was computed using the formula given by *Clay and Medwin* [1977, p. 98]. The pressure and boric acid contributions were dropped, since they are small for the depths and the frequency of interest. At 0.0°C and a salinity of 31.0, $\alpha = 5.97 \times 10^{-3} \text{ m}^{-1}$ at 192 kHz.

The rms acoustic backscatter amplitude, the rms temperature, and the rms salinity fine structure in the spreading plume are plotted in Figure 11 as functions of radial distance from the plume center. This plot was obtained by taking averages over the vertical extent of the spreading plume of all three quantities. We see a rapid fall-off in rms acoustic backscatter with distance from the plume center, and similar decreases in the rms temperature and salinity fine structure amplitudes.

4.4. Conservation Equations in the Spreading Plume

Conservation of volume in a thin cylindrical annulus of radius r and height h is given by

$$\frac{\partial}{\partial r} (Vhr) = 2W_e r \quad (12)$$

where W_e is an entrainment velocity, assumed to be the same at the upper and lower interfaces of the annulus, and V is the radial velocity. In an analogous fashion, we can write down the equation of conservation of point scatterers as

$$\frac{\partial}{\partial r} (CVhr) = 0 \quad (13)$$

where $C(r)$ represents the scatterer concentration and where it has been assumed that scatterers are neither entrained into

the spreading plume, nor removed from it. Combining (12) and (13) gives

$$\frac{\partial C}{\partial r} = \frac{-2W_e C}{Vh} \quad (14)$$

from which it is seen that in the absence of entrainment, $\partial C/\partial r = 0$, and we therefore conclude that the observed radial decay of acoustic backscatter cannot be explained by simple cylindrical spreading of conservative point scatterers.

If we now assume that the entrainment velocity is proportional to the radial velocity of the spreading plume, $W_e = \beta V$, where β is an entrainment coefficient, then (14) gives $h/2\beta$ as the radial decay scale for scatterer concentration. An estimate of β can be obtained from the overall Richardson number R_0 in the spreading plume, where R_0 is given by $-g\Delta\rho h/\rho_0 V^2$ assuming uniform flow in the spreading plume and zero horizontal velocity above and below, and where $\Delta\rho$ is the density difference across the plume boundaries. In order to estimate R_0 , we must first estimate V in the spreading plume. This is done by taking the vertical volume transport into the base of the spreading plume and equating it to the radial volume transport in the spreading plume. This procedure assumes that entrainment in the capping region and beyond is not significant, and in this sense our values of the Richardson number represent maximum estimates. For a vertical velocity of 30 cm/s and a plume width of 7 m (at approximately 20 m above bottom, using the computed widths in Figure 9), we get a total volume transport Q at the base of the spreading plume of $11.5 \text{ m}^3/\text{s}$. The horizontal velocity within the spreading plume is then $V = Q/2\pi rh$, and a value of 4 cm/s was obtained for CTD station 7, for which r is 9 m, and h is 5 m. Values for $\Delta\rho$ estimated from the upcasts and downcasts at the upper and lower plume boundaries were about 0.26 kg/m^3 for this station. These values give $R_0 = 7$. From experimental observations of two-dimensional density currents [*Ellison and Turner, 1959; Turner, 1973*], the entrainment coefficient β is approximately 5×10^{-5} for $R_0 \approx 7$. Thus $h/2\beta$ would be about $5 \times 10^4 \text{ m}$. However, this estimate is very sensitive to the choice for rising plume width, which enters the Richardson number inversely to the fourth power. For example, if the width at 20 m height were nearly doubled to 13 m, then $V \approx 14 \text{ cm/s}$ and $R_0 \approx 0.5$, giving $\beta \approx 5 \times 10^{-3}$ and $h/2\beta \approx 500 \text{ m}$. This is still much larger than the observed decay scale, so this analysis suggests that radial decay due to dilution of conservative point scatterers by entrainment is unlikely to explain the observed decay in the spreading plume.

We now consider the behavior of turbulence quantities, and begin with conservation of turbulent kinetic energy. Using Taylor's frozen field hypothesis and assuming no turbulence production (this is reexamined below), we consider the transport of turbulent kinetic energy (q^2) through a cylindrical annulus of radius r and thickness h and obtain

$$V(\partial q^2/\partial r) = \epsilon \quad (15)$$

where we have used (12) with W_e set to zero, since the fluid exterior to the spreading plume has been assumed to be nonturbulent. Equation (15) represents a balance between advection and dissipation and thus has the same form as the

energy budget for grid-generated turbulence [Tennekes and Lumley, 1972, p. 72], except that in this case the downstream distance is replaced by r .

Consider the time scale for the molecular dissipation of temperature fluctuations with scales of the order of one-half the acoustic wavelength. This time scale is given by $t_m = \lambda^2/4\gamma_T$, which is approximately 160 s using $10^{-7} \text{ m}^2/\text{s}$ for the thermal diffusivity (γ_T) in seawater. The maximum horizontal distance temperature fluctuations with this scale can travel is found from the integral

$$t = \int_{r_0}^r dr/V$$

where r_0 is the radius at which the spreading plume begins. Setting $V = Q/2\pi rh$, one finds that $r^2 = 2V_0 r_0 t + r_0^2$, provided that h is constant. Substituting 160 s for t , and taking $r_0 = 10 \text{ m}$ where $V_0 \approx 5$ to 15 cm/s from before, gives $r_{\text{max}} \approx 16$ to 24 m . This indicates that it is possible for turbulent fluctuations of this scale to exist for radial distances up to 24 m from the center of the plume before being dissipated by viscosity. This is consistent with the maximum horizontal extent of the spreading plume observed acoustically, which is about 75 m (Plate 1), since we have ignored both the cascade of energy from larger scales down to scales of the order of $\lambda/2$, and any turbulence production in the spreading plume, and in this sense the 16- to 24-m result represents a lower limit. It is also much closer to the observed value than the 500 to $5 \times 10^4 \text{ m}$ estimate based upon dilution of conservative point scatterers by entrainment.

When an isotropic scalar field is superimposed upon an isotropic turbulent velocity field which decays as one over the downstream distance, as in the case for grid-generated turbulence in a homogeneous fluid and as (15) suggests may be the case here, then from self-preservation arguments the decay of the mean square scalar concentration fluctuations such as temperature and salinity follow a $r^{-3/2}$ law [Hinze, 1975, p. 301]. Therefore the acoustic backscatter amplitude resulting from these fluctuations should drop off as $r^{-3/4}$, since backscatter amplitude is proportional to the square root of the mean square fluctuation amplitude.

In Figures 12a, 12b, and 12c the three rms fluctuation quantities in Figure 11 are plotted on a log-log scale. Figure 12d is a plot of acoustic backscatter amplitude versus radial distance from the plume axis. It was constructed from three acoustic transects through the plume, one of which corresponds to acoustic image A in Plate 1. The radial distance from the plume center was calculated for each position along the transect. The backscatter amplitudes were averaged in the vertical over a 1-m interval centered at a depth of 26 m, which corresponds approximately to the center of the spreading plume, and finally block averaged over 15 points or about 4 m in the horizontal. The solid and dashed lines in Figure 12 have slopes of $1/r$ and $1/r^{3/4}$, respectively. There is reasonable agreement between the acoustic backscatter amplitude and rms temperature decay rates and the $r^{-3/4}$ slope, whereas the salinity fine structure falls off more slowly. These results support the argument that turbulence contributes significantly to the observed acoustic backscatter, because of the agreement with the $r^{-3/4}$ slope and because acoustic refractive index fluctuations are expected to be affected more by temperature than by salinity.

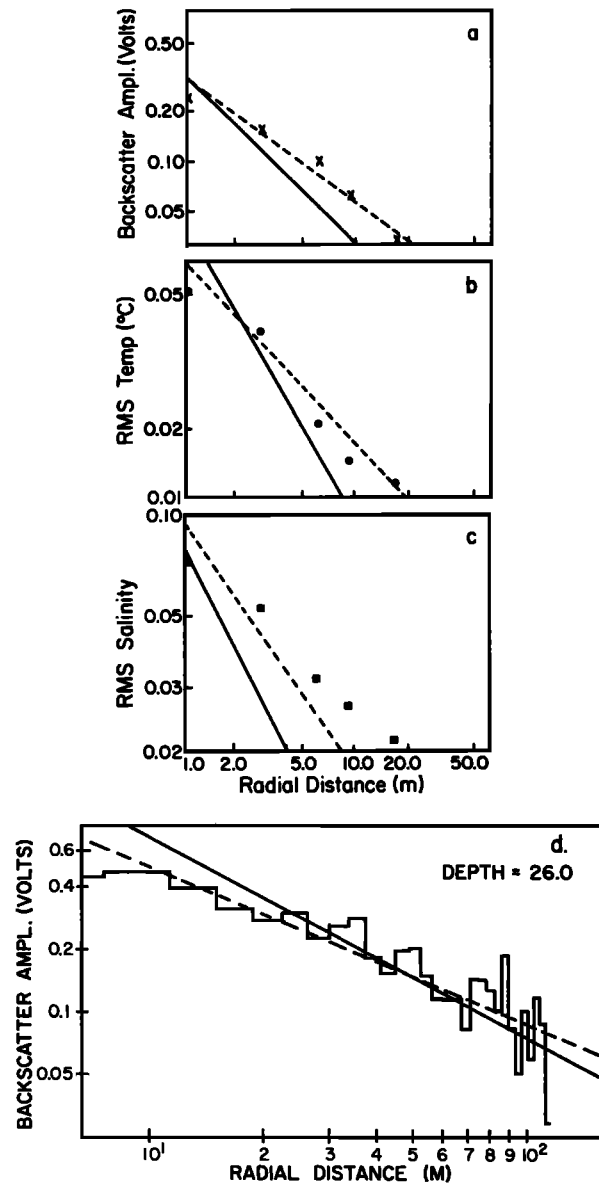


Fig. 12. Log-log plots of rms (a) backscatter amplitude, (b) temperature, and (c) salinity fluctuations shown in Figure 11, and (d) log-log plot of the rms acoustic backscatter amplitude in the spreading plume at a depth of 26 m obtained from the acoustic sounding transects. The solid and dashed lines are $1/r$ and $1/r^{3/4}$ drop-off rates.

4.5. Production and Dissipation in the Spreading Plume

Equation (15) is based on the assumption that turbulent production is unimportant in the spreading plume. To justify this, we estimate the gradient Richardson number Ri , given by

$$Ri = \frac{-g \Delta\rho \Delta z}{\rho_0 V^2} \quad (16)$$

assuming, as for R_0 , uniform flow in the spreading plume and zero horizontal velocity above and below. As before, $\Delta\rho$ is the density difference across the plume boundary, which has thickness Δz . Values of Ri were computed for CTD stations 8 and 7, located at distances of 6 and 9 m, respectively, from the plume center (Figure 3), and at which the plume thickness was 6 and 5 m. Using the volume transport argument

from the previous section, horizontal velocities of 5 and 4 cm/s were obtained. Typical values for $\Delta\rho$ and Δz obtained at the plume boundaries were 0.83 kg/m^3 and 0.92 m at $r = 6 \text{ m}$, and 0.26 kg/m^3 and 0.77 m at $r = 9 \text{ m}$, giving gradient Richardson numbers of 2.8 and 1.2. Again, however, these Richardson number estimates are very sensitive to the rising plume width, and doubling this width as before gives values of 0.18 and 0.08. The Reynolds numbers (Vh/ν) at these radial distances are in the range 10^5 – 10^6 . These results indicate that turbulence production probably occurs within the spreading plume because the Reynolds numbers are large and may occur at the plume boundaries for radial distances up to at least 10 m. The mean speed V decreases with radial distance, implying that the Reynolds number would decrease with radial distance and that the gradient Richardson number would increase but for the fact that $\Delta\rho$ must also decrease. So it is not clear at which distance production will definitely cease to be important.

Finally, we have been forced to ignore the possible contributions of internal waves to the observed fine structure and of internal wave radiation to the radial decay of turbulence quantities in the spreading plume. These processes have been examined in recent laboratory studies of the collapse of grid-generated turbulence in a stratified fluid [Stillinger *et al.*, 1983; Itsweire *et al.*, 1986], and would have to be taken into account in a complete treatment of the importance of turbulent mechanical energy production in the spreading plume.

4.6. Biological Implications

The benthic community associated with the freshwater spring and vent area is very productive compared with the surrounding area. The submersible observations revealed brilliantly colored sea anemones, kelp, scallops, shrimp, and other organisms at the vent itself (the large rock in Figure 6 was in fact almost completely covered with these organisms) and large soft corals on the periphery of the vent area. Elsewhere, life was sparse. The high density of benthic organisms is almost certainly related in part to the fact that the bottom in the discharge area is largely rocks and cobbles, while in the surrounding area it consists of fine-grained mud. The rock surfaces provide a substrate to which these organisms can attach themselves, and they are likely kept clean of detritus and other fine-grained material by the buoyant discharge. The near-bottom convergence zone is almost certainly important as well, providing a continuous flow of particulates entrained from the surrounding water past these filter-feeding organisms. This is also suggested by the presence of large (1 m high) branching soft corals which we found ringing the discharge area, at an estimated distance of 5 to 10 m from the center. These corals were found nowhere else.

The rising plume may also represent a source of nutrients for the upper layer. Figure 13 shows sections of nutrients and dissolved O_2 from the 1983 survey. The upper 50 m of the water column has been stripped of nutrients, most likely as a result of primary production earlier in the year. (Note also the depleted oxygen levels and higher nitrate and silicate concentrations at depth behind the sill, 15 km from the head). The vertical flux of nutrients in the plume can be estimated using the concentrations in Figure 13. If for example we take a vertical velocity of 30 cm/s and the nitrate concentration at 50 m depth, approximately $3 \mu\text{g-at/L}$, then

the vertical flux of nitrate would be about $10^3 \mu\text{g-at/m}^2/\text{s}$. This plume flux may be compared with the diffusive flux to be expected at 50 m depth in the rest of the fjord. Using the value of $N = 10^{-2} \text{ s}^{-1}$ from section 4.1, we obtain $10^{-5} \text{ m}^2/\text{s}$ for the apparent diffusivity from the values compiled by Broecker [1981, Figure 15.19]. Since the nitrate gradient at 50 m depth in Figure 13 is about $2 \times 10^2 \mu\text{g-at/m}^4$, the diffusive flux of nitrate should be about $2 \times 10^{-3} \mu\text{g-at/m}^2/\text{s}$, which is nearly 6 orders of magnitude smaller than the estimated plume flux. Furthermore, the plume flux could at times be much larger if coupling with baroclinic motions, involving upward displacement of the density field at the head, were considered. These calculations suggest that the plume must represent an important nutrient source that might sustain primary production locally at much higher levels than are possible in the rest of the fjord, after the initial phytoplankton blooms have stripped the nutrients from the upper layer.

5. SUMMARY AND CONCLUSIONS

Results from a 3-day field study of the Cambridge Fiord submarine spring and buoyant plume have been presented. Measurements made from a launch using a 192-kHz acoustic sounder and a grid of CTD stations, together with CTD and current meter measurements made at the vent from a submersible, are used as a basis for comparison with numerical results from a buoyant plume model. Comparisons are also made between the rms acoustic backscatter amplitude and the rms temperature and salinity fine structure amplitudes, in the neutrally buoyant spreading plume. Finally, a productive benthic community discovered in the vent area has been described, and it has been remarked that the plume may have an important influence on the nutrient supply to the euphotic zone at the head of Cambridge Fiord.

The submersible observations show that the discharge region is about 5 m in horizontal extent, with several smaller points of discharge nearby. The freshwater discharge does not stream freely from the bottom, instead converging along the bottom toward the center of the vent area before acquiring much vertical momentum. Mixing of the discharged water with ambient seawater occurs within this convergent flow, and the initial geometry is further complicated by a large rock sitting in the middle of the discharge area.

Ditmars' [1969] plume model uses axisymmetric, horizontally integrated conservation equations and assumes that the radial profiles of velocity and density are Gaussian. Entrainment of ambient fluid into the rising plume is assumed to be proportional to the centerline velocity. The model is initialized at 1 m above the bottom, where the flow was found to be plume-like and is assumed to be fully developed. For initial salinities comparable to those measured from the submersible at about this height above bottom, the observed maximum height of rise provides a lower limit to the possible freshwater discharge: $0.1 \text{ m}^3/\text{s}$. Lower discharge rates yield computed heights of rise less than that observed. Because of the capping effect of the near-surface low-salinity layer, however, the observed height of rise does not provide a realistic constraint on the maximum possible freshwater discharge. This constraint is provided instead by the plume width 1 m above bottom, which the submersible observations indicate is less than 5 m, and yields $0.2 \text{ m}^3/\text{s}$ as the

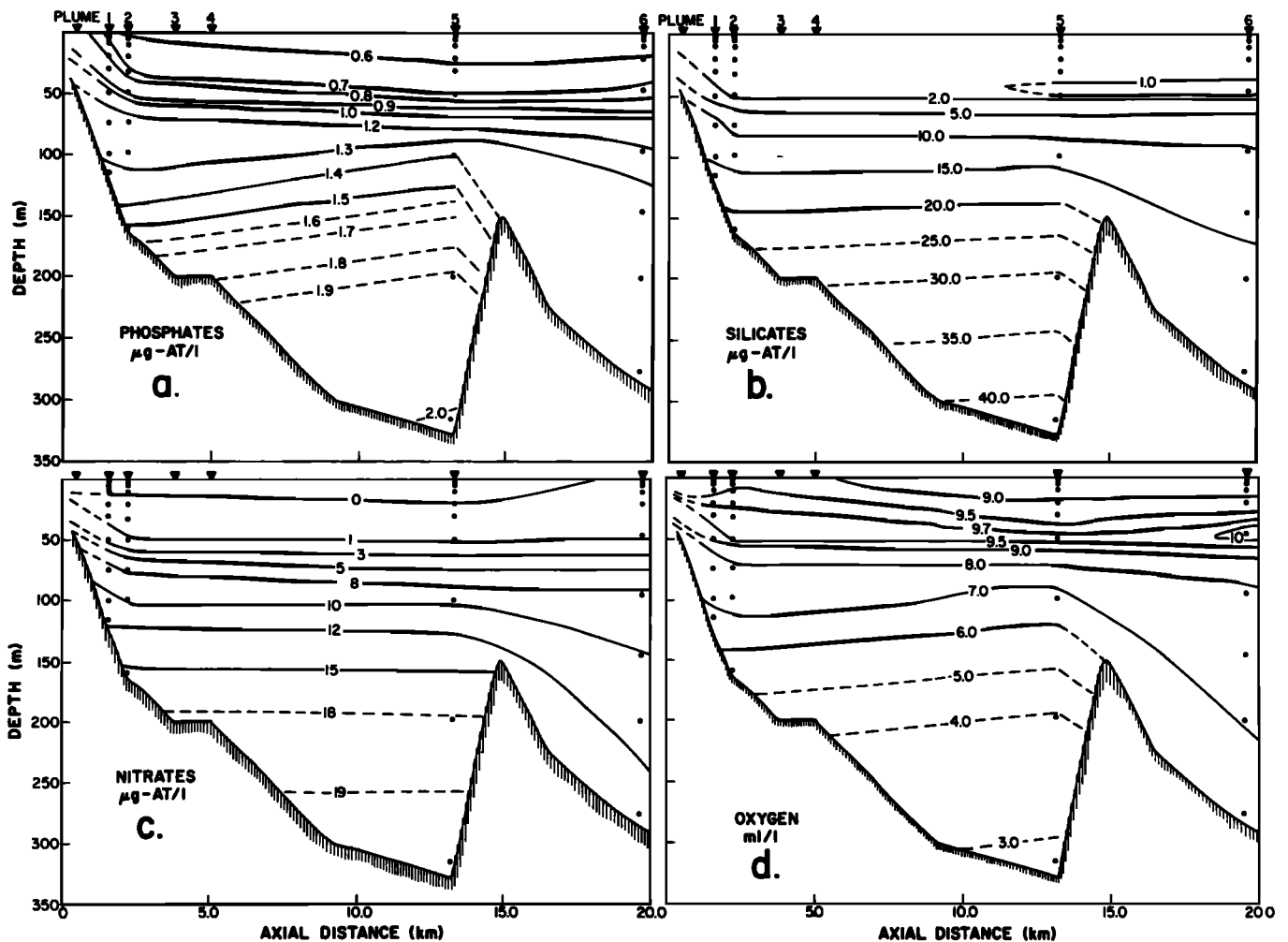


Fig. 13. Vertical sections of nutrients and dissolved oxygen at the head of the fjord, from 1983. The solid circles represent sample positions.

probable upper limit. This range of freshwater discharge rates is comparable to the $0.14 \text{ m}^3/\text{s}$ estimate made by *Sadler and Serson* [1980], and is consistent with the 1.0 to 2.0 m decrease in the water level of the lake on the delta during winter.

The centerline vertical velocities from the model are significantly greater (up to a factor of 2) than the values obtained in the same depth range from the slopes of rising scatterer trajectories in acoustic images acquired while the launch was moored over the rising plume. Since the mechanism responsible for these recurrent, coherent, scattering structures has not been established, the reason for the discrepancy is not known. However, it does seem reasonable to point out that a possible generating mechanism for the scattering structures is the formation of large eddies at the edge of the plume through a convective or shear instability, and that such eddies would rise more slowly than the centerline rate. This would explain the speed discrepancy.

Several studies [*Munk and Garrett*, 1973; *Proni and Apel*, 1975; *Goodman and Kemp*, 1981] have suggested that turbulent microstructure may cause acoustic backscatter at detectable levels in the ocean. We conclude here that turbulent microstructure may well be responsible for the observed acoustic backscatter from the plume. This conclu-

sion is based mainly on the observation that the radial decay of rms acoustic backscatter and the rms temperature fine structure are comparable in the spreading plume. Furthermore, the observed radial decay scale appears to be explicable by assuming a balance between advection and diffusion of mean square turbulence quantities, and finally, this balance yields an $r^{-3/4}$ dependence, which is consistent with the measurements. Nevertheless, these results are only suggestive. Definitive answers would require microstructure measurements as a function of radial distance in the spreading plume at least, and measurements of mean field quantities, including mean velocity, would clearly be useful. Both were beyond the scope of this study. The results obtained here do indicate, however, that such experiments could shed light not only on the problem of detecting turbulent microstructure acoustically in the ocean but also on the general problem of the collapse of turbulence from a quasi-steady source of turbulence in the presence of stratification.

Acknowledgments. We thank the crews of the *Pandora II* and the submersible *Pisces IV*, and J. Foley and A. Walsh, for their assistance during the field program, and A. Kucherra and M. Sullivan for help with the image processing. The Keck Laboratory of Hydraulics and Water Resources at the California Institute of

Technology provided the computer code for the buoyant plume model. We also thank R. Trites of the Bedford Institute of Oceanography for making the portable CTD available to us, and L. Petrie for help with the data translation. The Atlantic Geoscience Center provided the microwave positioning system. This project was supported by grants from the Natural Sciences and Engineering Research Council, the Department of Energy Mines and Resources Canada, and the Department of Fisheries and Oceans Canada.

REFERENCES

- Blume, H. J. C., B. M. Kendall, and J. C. Fedors, Multifrequency radiometer detection of submarine freshwater sources along the Puerto Rican coastline, *J. Geophys. Res.*, 86(C6), 5283–5291, 1981.
- Broecker, W. S., Geochemical tracers and ocean circulation, in *Evolution of Physical Oceanography*, edited by B. A. Warren and C. Wunsch, pp. 434–460, MIT Press, Cambridge, Mass., 1981.
- Clay, C. S., and H. Medwin, *Acoustical Oceanography*, 544 pp., John Wiley, New York, 1977.
- Colbourne, E. B., An acoustic remote sensing study of an Arctic submarine spring, MSc. thesis, Memorial Univ. of Newfoundland, St. John's, Canada, 1987.
- Colbourne, E. B., and A. E. Hay, Remote acoustic mapping of a submarine spring plume, in *Progress in Underwater Acoustics*, edited by H. M. Merklinger, pp. 207–213, Plenum, New York, 1987.
- Ditmars, J. D., Computer program for round buoyant jets into stratified ambient environments, *Tech. Memor. 69-1*, W. M. Keck Lab., Calif. Inst. of Technol., Pasadena, March 1969.
- Dunbar, M., Curious open water feature in the ice at the head of Cambridge Fiord, in *Comptes Rendus et Rapports, Assemblée Generale de Toronto*, vol. 4, pp. 514–519, Societe Inter nationale de Géographie, Gentbrugge, Belgium, 1958.
- Ellison, T. H., and J. S. Turner, Turbulent entrainment in stratified flows, *J. Fluid Mech.*, 6, 423–448, 1959.
- Fan, L. N., and N. H. Brooks, Numerical solutions of turbulent buoyant jet problems, *Rep. KH-R-18*, W. M. Keck Lab., Calif. Inst. of Technol., Pasadena, Jan. 1969.
- Farmer, D. M., and J. D. Smith, Tidal interactions of stratified flow with a sill in Knight Inlet, *Deep Sea Res.*, 27, 239–254, 1980.
- Fischer, H. B., E. J. List, R. C. Y. Koh, J. Imberger, and N. H. Brooks, *Mixing in Inland and Coastal Waters*, 483 pp., Academic, San Diego, Calif., 1979.
- Gill, A. E., *Atmosphere-Ocean Dynamics*, Academic, San Diego, Calif., 1982.
- Goodman, L., and K. Kemp, Scattering from volume variability, *J. Geophys. Res.*, 86(C5), 4083–4088, 1981.
- Haury, L. R., M. C. Briscoe, and M. H. Orr, Tidally generated internal wave packets in Massachusetts Bay, U.S.A., *Nature*, 278, 312–317, 1979.
- Hay, A. E., Remote acoustic imaging of the plume from a submarine spring in an Arctic fiord, *Science*, 255, 1154–1156, 1984.
- Hinze, J. O., *Turbulence*, McGraw-Hill, New York, 1975.
- Itswire, E. C., K. N. Helland, and C. W. Van Atta, The evolution of grid-generated turbulence in a stably stratified fluid, *J. Fluid Mech.*, 162, 299–338, 1986.
- Kaye, G. T., Correlation between acoustic scatterers and temperature gradients, *J. Mar. Res.*, 37, 319–326, 1979.
- Kohout, F. A., Submarine springs: A neglected phenomenon of coastal hydrology, paper presented at Symposium on Hydrology and Water Resources Development, Central Treaty Organ., Ankara Feb. 5–12, 1966.
- List, E. J., Turbulent jets and plumes, *Annu. Rev. Fluid Mech.*, 14, 189–212, 1982.
- Mackenzie, K., Nine term equation for sound speed in the oceans, *J. Acoust. Soc. Am.*, 70, 807–812, 1981.
- Manheim, F. T., Evidence for submarine discharge of water on the Atlantic continental slope of the southern United States, and suggestions for further work, *Trans. N. Y. Acad. Sci.*, 29, 839–853, 1967.
- Morton, B. R., Forced plumes, *J. Fluid Mech.*, 5, 151–163, 1959.
- Morton, B. R., G. I. Taylor, and J. S. Turner, Turbulent gravitational convection from maintained and instantaneous sources, *Proc. R. Soc. London, Ser. A.*, 234, 1–23, 1956.
- Munk, W., and C. Garrett, Internal wave breaking and microstructure, *Boundary Layer Meteorol.*, 4(37), 1973.
- Palmer, D. R., and P. A. Rona, Acoustic imaging of high temperature hydrothermal plumes at seafloor spreading centers, *J. Acoust. Soc. Am.*, 80(3), 888, 1986.
- Pelech, I., G. G. Zipfel, and R. L. Holford, A wake scattering experiment in thermally stratified water, *J. Acoust. Soc. Am.*, 73, 528–538, 1983.
- Petrie, W. M., and R. W. Trites, Synoptic Oceanography of Baffin Island fjords, Sedimentology of Arctic Fiords, compiled by J. P. Syvitsky, chap. 2, *Can. Data Rep. Hydrogr. Ocean Sci.*, 28(2), 1–63, 1984.
- Proni, J. R., and J. R. Apel, On the use of high frequency acoustics for the study of internal waves and microstructure, *J. Geophys. Res.*, 80, 1147–1151, 1975.
- Sadler, H., and H. Serson, An unusual polynya in an Arctic fiord, in *Fiord Oceanography*, edited by H. Freeland et al., pp. 299–304, Plenum, New York, 1980.
- Stillinger, D. C., K. N. Helland, and C. W. Van Atta, Experiments on the transition of homogeneous turbulence to internal waves in a stratified fluid, *J. Fluid Mech.*, 131, 91–122, 1983.
- Tatarski, V., *Wave Propagation in a Turbulent Medium*, p. 68, Dover, New York, 1961.
- Tennekes, H., and J. Lumley, *A First Course in Turbulence*, 300 pp., MIT Press, Cambridge, Mass., 1972.
- Thorpe, S., and J. Brubaker, Observations of sound reflection by temperature microstructure, *Limnol. Oceanogr.*, 28, 601–613, 1983.
- Turner, J. S., *Buoyancy Effects in Fluids*, 368 pp., Cambridge University Press, New York, 1973.
- Turner, J. S., Turbulent entrainment: the development of the entrainment assumption, and its application to geophysical flows, *J. Fluid Mech.*, 173, 431–471, 1986.

E. B. Colbourne, Department of Fisheries and Oceans, P.O. Box 5667, St. John's, Newfoundland, Canada A1C 5X1.

A. E. Hay, Department of Physics, Memorial University of Newfoundland, St. John's, Newfoundland, Canada A1B 3X7.

(Received July 10, 1989;
accepted October 30, 1989.)

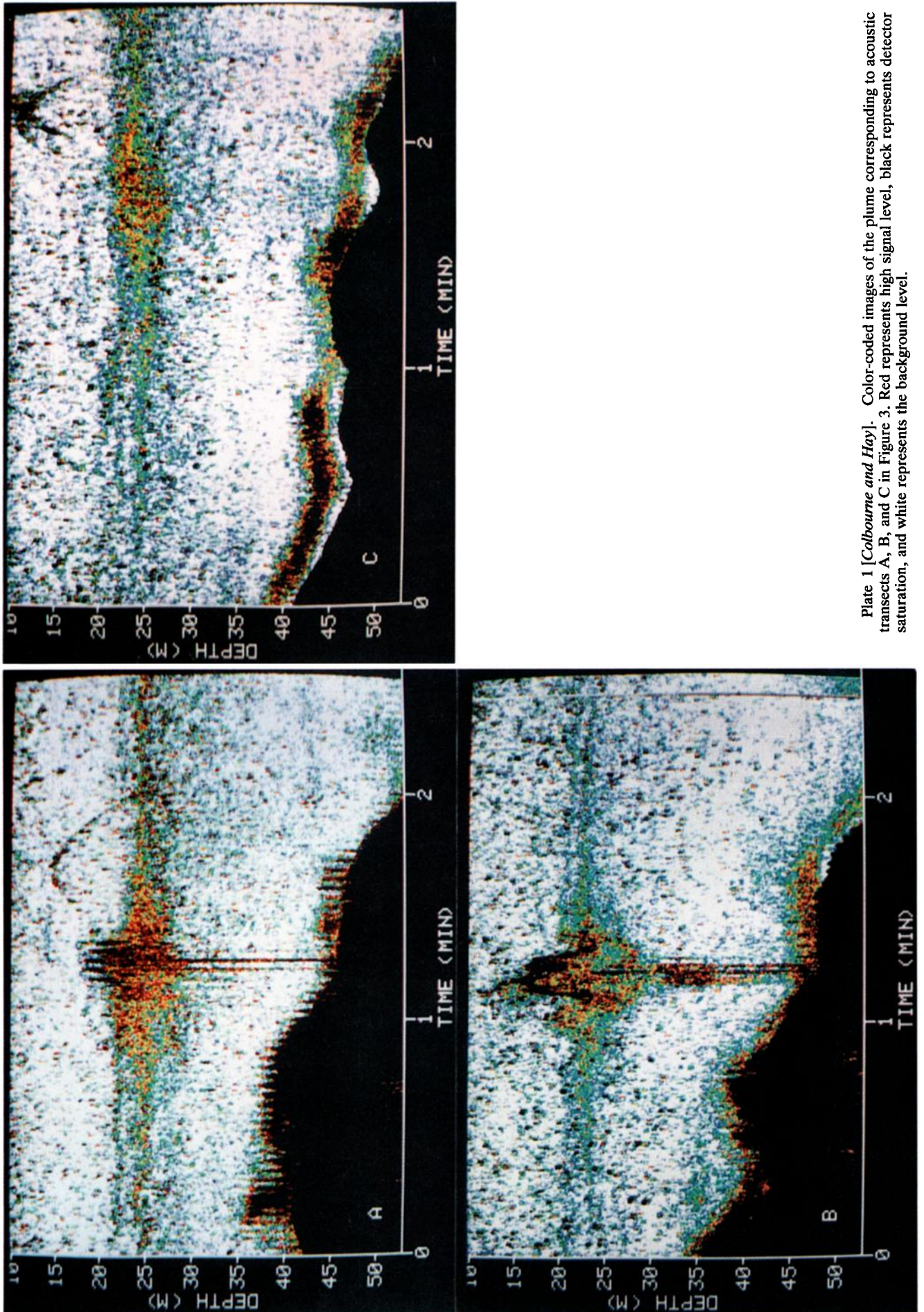


Plate 1 [Colbourne and Hay]. Color-coded images of the plume corresponding to acoustic transects A, B, and C in Figure 3. Red represents high signal level, black represents detector saturation, and white represents the background level.

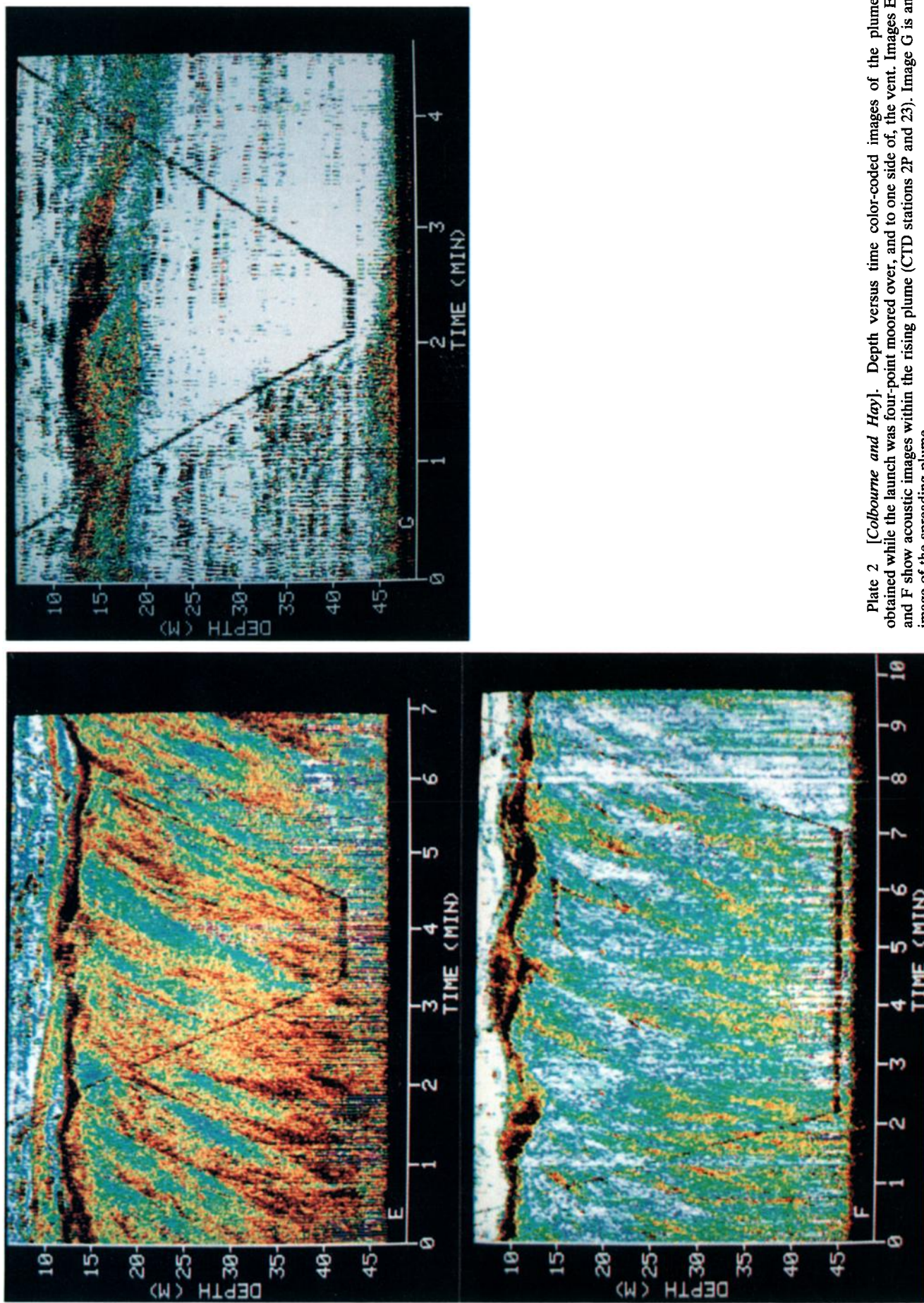


Plate 2 [Colbourne and Hay]. Depth versus time color-coded images of the plume obtained while the launch was four-point moored over, and to one side of, the vent. Images E and F show acoustic images within the rising plume (CTD stations 2P and 23). Image G is an image of the spreading plume.